

On Two-Dimensional Steady-States of Supersonic Flows Over Compression Ramps and their Global Linear Instability

Ricardo Dias dos Santos,* and Leonardo Santos de Brito Alves†
Universidade Federal Fluminense, Passo da Pátria 156, Rio de Janeiro, Brazil

Nicolas Cerulus‡
University of Liverpool, Brownlow Hill, England, L69 3GH, United Kingdom

Vassilis Theofilis§
University of Liverpool, Brownlow Hill, England, L69 3GH, United Kingdom
and
Universidade Federal Fluminense, Passo da Pátria 156, Rio de Janeiro, Brazil

This work is motivated by planned three-dimensional global linear stability analyses of supersonic laminar two-dimensional flows over compression ramps. Spatially accurate and temporally converged two-dimensional base flows are a necessary condition for the generation of reliable instability analysis results. Two complementary tools are utilized, namely a second-order accurate compressible solver as implemented in OpenFOAM and a recently developed in-house second-order finite-difference TVD code. Both codes use an explicit Euler marching scheme. Although spatially converged results have been obtained with both codes, resolving a domain that includes a flat plate with a rounded leading edge and a substantial portion of the attached boundary layer downstream of the ramp with $O(10^6)$ elements, as expected, the in-house code obtains results of comparable quality within substantially smaller computer times. However, both codes, independently, reveal well-resolved temporal oscillations which appear to be of physical origin and may be linked with linear instability, even though these simulations were performed under parametric conditions previously thought to be stable. This indicates a need for the development of new methods that allow the generation of steady-states that have imbedded discontinuities, such as shock waves. Two-dimensional global mode analyses performed herein indicate the essential role played by the shock in linear instability of compression ramp flows, the amplitude functions linking together, via their respective peaks, the compression shock and the laminar recirculation bubble. This result is well-known from the classic two-dimensional global instability analysis of turbulent flow over a transonic wing and has recently also been documented in laminar shock-dominated flow of a double cone flow in the hypersonic regime.

I. Introduction

Separation generated in supersonic and hypersonic flat-plate boundary layers due to an impinging shock (system) associated with various-shaped deviations from the flat geometry, such as the planar compression ramp, schematically depicted in Fig. 1, or similar axisymmetric configurations, have all been the subject of intense investigations ever since the early experimental works of Chapman *et al.* [1, 2] recognized the significance of separation to the laminar-turbulent transition process at high speeds. In turn, correct prediction of the instability dynamics of flow separation is key to the exact determination of the relative portions of laminar and turbulent flow on parts of a vehicle traveling at supersonic and hypersonic speeds. They are required for the subsequent correct prediction of heat transfer through the surface of vehicle parts that are critical to aerodynamic performance.

Canonical cases studied in this context include separation induced by shocks impinging on laminar or turbulent boundary layers on the flat plate, separation caused by forward- or backward-facing steps, or roughness elements

*Ph.D. Student, Mech. Engr. Dept., ricardos@id.uff.br

†Professor, Mech. Engr. Dept., AIAA Member, leonardo.alves@mec.uff.br

‡Research Assistant, School of Engineering, N.Cerulus@student.liverpool.ac.uk

§Chair in Aerospace Engineering, School of Engineering, Associate Fellow, v.theofilis@liverpool.ac.uk

embedded inside the boundary layer, having a size of the order of the local boundary layer thickness, as well as separation localized at small- and finite-angle, two-dimensional or oblique wedges. Edney [3] documented experimentally and classified a number of patterns arising in shock-induced separation, Babinsky and Harvey [4] present an overview of the observed phenomena, while Gaitonde [5] recently discussed progress made in understanding this class of flows. A key issue identified is the low-frequency shock oscillation, purported in the literature to be associated with some form of linear flow instability. Understanding the precise nature of this instability, as well as its dependence on the underlying base or mean flow parameters, would close the currently open debate on this topic and also open up avenues to pursue flow control via control of flow instabilities. The latter approach is widely accepted to be the most efficient, from an energy-balance point of view, theoretically founded flow control methodology [6] which has been employed successfully in a wide range of applications of aeronautical interest [7].

Early numerical solutions to the compression ramp problem were obtained by Carter [8] and Hung and MacCormack [9], Kutler and Shankar [10] and Shankar *et al.* [11], while the work of Rudy *et al.* [12] compared results obtained on this problem by finite-difference and finite-volume solvers available in the literature up to that time. Results obtained established that the interaction of the shock with the leading edge induces the formation of an expansion fan through Edney type VI interactions, while for hypersonic flows surface pressures were found to be higher than those calculated using inviscid shockwave theory [9].

More recently, experiments have been used in conjunction with numerical work, in order to validate and compare the flowfields obtained. Zapryagaev *et al.* [13] studied three-dimensional laminar compression ramp flows at $M_\infty = 6.01$, $p_0 = 9.73 \times 10^5$ Pa, $T_0 = 380$ K and $Re_L = 6 \times 10^5$ at a ramp angle $\alpha = 30^\circ$. Numerically the flow was studied using an 8.9 million element grid refined near the wall, using a second-order in space and first-order in time upwind differencing scheme. Good agreement between numerical and experimental results was obtained, and the three-dimensional nature of the flow through spanwise separation on the plate was confirmed. A mass discharge region was also observed, where the freestream fluid flowed continuously into the separation region and back out through the side boundaries of the separated region [13].

Chuvakov *et al.* [14] also studied a nominally 2D laminar case both experimentally and numerically, aiming at understanding the effect of leading edge bluntness on the formation of the shockwaves. Experiments were performed in a Ludwieg tube at free stream $M_\infty = 8$ and $T_0 \approx 760$ K, covering a range of Reynolds numbers $Re_L = 0.15 \times 10^6 - 2.55 \times 10^6$. The geometry was also varied with different ramp lengths $L = 50$ & 150 mm as well as ramp angles $15^\circ \leq \alpha \leq 25^\circ$. A specific set of parameters was subsequently studied numerically using a Godunov type finite volume scheme. The conditions for the numerical work were, $\alpha = 15^\circ$, $Re_L = 3.71 \times 10^5$ and $L = 50$ mm. Again a range of leading edge bluntness' was studied and steady-states were obtained in a time of $\approx 40ms$. Overall good agreement between experimental and numerical work was demonstrated and multiple interesting phenomena were identified, notably the presence of vortices downstream of the separation region and the effect of leading edge bluntness on the entropy layer.

In preparation for a systematic analysis of linear instabilities in the compression ramp, the issue of accurate recovery of steady two-dimensional base flows must be addressed. The present effort compares laminar base flow results obtained by two separate codes, both using explicit Euler time marching schemes as well as second-order spatial discretizations that employ upwind TVD schemes for inviscid terms and central schemes for diffusion terms. One is the finite-volume methodology implemented in the OpenFOAM open source code whereas the other is an in-house finite-differences code based on generalized coordinates. Section II describes the finite-volume approach, its verification using the supersonic flow around a parabolic cylinder and results for the compression ramp problem. This is followed by section III, which describes the finite differences approaches, their verification using the supersonic flow around a circular cylinder and results for the same compression ramp. Both sections highlight the difficulties in obtaining steady-states with traditional explicit time integration schemes. Section IV presents results on the least-damped two-dimensional global modes associated with the base states computed herein. All amplitude functions highlight the intimate connection between the compression shock and the laminar separation zone, as has been seen in several recent global instability analyses of both laminar and turbulent separated flows. Preliminary conclusions of this on-going effort are summarized in section V.

II. OpenFOAM results

A. Numerical setup

Flow over a two-dimensional parabolic cylinder body, for which analytical results are known [15, 16], serves to assess resolutions necessary in the neighborhood of the leading edge of the flat plate in the compression ramp. Following a discussion by [17] the *rhoCentralFoam* solver has been used, all flow quantities being dimensional. In this respect it is interesting to recapitulate here the scalings used in this solver.

B. Verification with the parabolic cylinder

Physical parameters are set following the ideal gas law for air, $p = \rho R^* T$, in which the incoming stream pressure and temperature are set to $p_{inf} = 105660 \text{ Pa}$ and $T_{inf} = 300 \text{ K}$, respectively. Using the specific gas constant $R^* = 287.056 \text{ J kg}^{-1} \text{ K}^{-1}$ the incoming air density is determined and, alongside a ratio of specific heats $\gamma = 1.4$, the speed of sound $a = \sqrt{\gamma R^* T}$ can also be calculated. The target Mach number $Ma = 3.5$ is then used to compute the incoming flow speed $U_{inf} = 1215.16 \text{ m/s}$. Other parameters set in the solver are a molar weight $m = 28.9 \text{ kg/mol}$, implying treatment of air as diatomic gas, a specific heat at constant pressure, $c_p = 1005 \text{ J kg}^{-1} \text{ K}^{-1}$ and flow enthalpy $h_f = 5 \times 10^6 \text{ J kg}^{-1}$. Some experimentation has been conducted with the solvers used in the code, before settling for the set-up shown in the appendix. Simulations were performed with a $\text{CFL} \leq 0.1$, which determined an adjustable time-step of $O(10^{-11})\text{s}$.

The parabolic cylinder geometry is analytical, $f(x) = x^{\frac{1}{2}}$, and the solution domain is constructed using GMSH [18] and is decomposed in three sub-domains, such that the structured elements constructed be approximately rectangular, as schematically shown in Figure 2. In the left part of this figure it can be seen that both the cylinder surface and the inflow boundaries have been constructed analytically (using cubic splines) and that a common wall-normal discretization and independent spatial discretizations in the direction along the surface are used; a rather low resolution is used in this image, for visualization purposes. In the right part of the same image, the pressure distribution at steady state is shown. Steadiness is monitored by probing solution values as a function of time at arbitrarily chosen locations in the flowfield. Figure 3 shows a typical evolution of the flow variables at a probe placed at $(x_p, y_p) = (-0.1, 0.1)$. It is immediately obvious that, while velocity appears to attain a steady state value at a rather short time after the shock passage and rebound on the body surface, it takes substantially longer for flow quantities to relax to true steady states. Table 1 shows the values of these steady states at a time $t = 0.1\text{s}$, a time at which converged of the first three significant digits can be ascertained on the two higher-density grids. The conclusion drawn here is that a grid comprising $O(9 \times 10^4)$ elements is needed in order to resolve this flow, a value which is consistent with that presented by [17], and can be used as guidance for the resolutions needed in the compression ramp.

C. Verification with the viscous flow over a compression ramp

A systematic grid convergence study was performed in order to generate reference solutions for this geometry. Experience gained in the parabolic cylinder as regards meshing parameters at the supersonic conditions monitored has guided the construction of a simulation domain in which a rounded leading edge preceded the flat plate, in order to eliminate singularities that could condition solution convergence; Fig. 4 presents details of the geometry. A coarse version of the structured grid used for the OpenFOAM ramp simulations is shown in Figure 5 for illustration purposes.

The *rhoCentralFoam* solver has next been used to resolve viscous flow over the compression ramp. Besides the setup of physical parameters discussed in the previous section, Sutherland's law

$$\mu = C_s \times \left(\frac{T^{3/2}}{T + T_s} \right) \quad \text{where} \quad C_s = \mu_0 \times \left(\frac{T_0 + S}{T_0^{3/2}} \right) \quad , \quad (1)$$

has been used to calculate the dynamic viscosity with constant values $C_s = 1.4586 \times 10^{-6} \text{ Pa K}^{-\frac{1}{2}}$ and $T_s = 110.4 \text{ K}$; the remaining free-stream parameter values used in the present simulations are shown in Table 5. Table 2 presents the steady streamwise velocity component obtained with $O(0.7 \times 10^6)$, $O(3 \times 10^6)$ and $O(7 \times 10^6)$ grid elements at three probe locations inside the boundary layer, namely $(x_1 = 5 \times 10^{-5}, y_1 = 10^{-5})$, prior to the laminar separation bubble, $(x_2 = 10^{-3}, y_2 = 10^{-5})$, inside the laminar separation zone at the ramp junction, and $(x_3 = 1.2 \times 10^{-3}, y_3 = 10^{-4})$, on the downstream ramp wall. These results show that the solution is not yet converged, especially prior to the separation bubble. The reason, however, does not seem to be attributed to poor spatial resolution, as will be discussed shortly. Table 3 shows that integral quantities, such as the location of primary separation and primary reattachment, are predicted

reasonably well on either of the three grids defined in this table; Fig. 5 also shows the distribution of skin friction coefficient with distance from the ramp corner on each of these grids and offers visual confirmation of the apparent spatial convergence of the solutions.

Returning to the question of temporal convergence, Figure 6 shows short and long time histories to the same velocity component before, at and after the separation bubble. After a nonlinear initial stage caused by inaccurate initial conditions, the signal becomes smooth after approximately $10\mu s$. However, between $75\mu s < t < 150\mu s$, depending on the measurement location, disturbances can be observed to grow and saturate, reaching a statistically stationary steady-state whose unsteady signal oscillates with a high frequency. This can be observed in spatial profiles as well. Figure 7 shows the streamwise velocity component and pressure variations normal to the wall at different streamwise locations along the ramp. Although the former is reasonably smooth, the latter does present small amplitude high wavenumber oscillations. In other words, it was not possible to reach a true steady-state using OpenFOAM under the temporal and spatial resolutions, as well as parametric conditions, employed. Figure 8 presents evidence of this statement in terms of the gradient of the velocity magnitude of the computed solution, in which well-resolved small-amplitude oscillations are visible to emanate at the shock and the vicinity of the leading-edge and extend over the entire solution domain. It is conceivable that these oscillations have physical origin and it is also likely that the resolutions issues encountered both in the OpenFOAM simulations discussed and the simulations using the in-house code that follow are related with these oscillations being better resolved and certainly remaining active in the solution as resolution is increased.

III. In house code results

A. Numerical setup

In order to further examine this difficulty with the generation of steady-states observed with OpenFOAM, two high-order finite difference codes, parallelized using PETSc library [19], were written with the ability to deal with complex geometries. One used generalized coordinates and the other Cartesian coordinates with the cut-stencil method [20]. Inviscid terms used the Roe's flux difference scheme [21] combined with second-order accurate TVD (Total Variation Diminishing) scheme [22], whereas viscous terms used a conservative second-order central differences scheme. Since steady-states are the goal here, time integration was performed with an explicit Euler scheme.

B. Verification with the circular cylinder

These codes are also verified for the flow around a circular cylinder [23]. The dimensionless parametric conditions are the same ones used for the parabolic cylinder simulated with OpenFOAM, even though the cylinder geometry is circular with a diameter of $D = 2 m$. Table 4 shows that $O(2 \times 10^5)$ grid points are sufficient to graphically converge all important variables. Using this number of grid points, the pressure iso-contours agree very well with the literature [23], as shown in Figure 9 (left). The right plot in this same figure shows the temporal behavior of the steady-state residue maximum norm over the entire domain. Assuming $\partial\mathbf{q}/\partial t = \mathbf{f}(\mathbf{q})$ is the system of equations being solved in vector form, $\mathbf{f}(\mathbf{q})$ is the steady-state residue. Hence, a steady-state \mathbf{q}_s is obtained when $\mathbf{f}(\mathbf{q}_s) \approx 0$. Figure 9 (right) shows that this residue decreases approximately 14 orders of magnitude before reaching machine precision, clearly indicating that a steady-state was reached for this problem. It is important to note high frequency oscillations during early times, as observed in the OpenFOAM simulations, which transition to low frequency oscillations before reaching a steady convergence rate towards steady-state. Although not shown here, a cut-stencil Cartesian coordinates version of this code produces very similar results.

C. Verification with the viscous flow over a compression ramp

The viscous flow over a compression ramp simulated with OpenFOAM was also simulated with the in-house codes under the same dimensionless parametric conditions of the stable laminar flows reported by Carter [8], which used Sutherland's law with $T_0 = 273.11K$ and $S = 110.56K$ instead, where μ_0 is given by Table 5. The generalized coordinate transformation employed for the compression ramp in this code is the one used by Martin *et al.* [24] for the same problem, but with the near wall grid clustering parameter equal to $\eta_1 = 0.6, 0.7$ and 0.8 , as shown in Figure 10. These authors used a slightly weaker grid clustering, with $\eta_1 = 0.5$. All results presented here for the in-house code used time step of $\Delta t = 10^{-7} s$ and a distance between leading edge and corner equal to $L = 10 m$, such that the Reynolds number matches that used in the OpenFOAM analysis.

A comparison with the wall-pressure distribution from Carter is shown in Figure 11 for different grids generated

with $\eta_1 = 0.7$ and extracted at $t = 0.05$ s. There is a qualitative agreement between the results from Carter and the present results, although quantitative differences tend to become larger as the number of grid points used by the in-house code increase. Furthermore, the wall-pressure curve obtained with $N_x = 3001$ and $N_y = 1001$ is essentially identical to the one obtained with $N_x = 3601$ and $N_y = 1201$, indicating that $N_x = 3001$ might be a sufficient number of grid points in the streamwise direction near the shock boundary-layer interaction region ($x/L \approx 0.94$). Density (left), pressure (middle) and temperature (right) profiles in the wall normal direction, measured at $t = 0.05$ s and $x/L = 1$, are shown in Figure 12. They indicate that these profiles are not yet grid converged, however, although only slightly so. These profiles are also more sensitive to the grid refinement level than to the number of grid points. Nevertheless, this figure shows that $N_y = 1201$ and $\eta_1 = 0.8$ does not likely lead to grid converged results in the wall normal direction.

Despite this lack of grid convergence, Figure 13 (left) shows the streamwise velocity (top) and temperature (bottom) iso-contours for the parametric conditions CR1 in Table 5 to be in qualitative agreement with the literature and the OpenFOAM results in Figure 7. The impact of this lack of grid convergence, on the other hand, can be observed on the right plot in Figure 13, which shows the density increment (mass conservation residue multiplied by Δt) maximum norm over the entire domain versus time for a different number of grid points and of grid refinements. This figure shows that this residue drops between 2 and 3 orders of magnitude before reaching an approximate statistically stationary state between $0.05 < t < 0.06$ s, independent of the number of grid points and the level of grid refinement. Figure 12 (left) might explain why. The maximum density error according to this figure is $O(10^{-2} \text{ kg/m}^3)$, which likely prevents the maximum density increment shown in Figure 13 (right) from reaching magnitudes smaller than $O(10^{-3} \text{ kg/m}^3)$.

Even though the density increment seems to be statistically stationary within $0.06 < t < 0.09$ s, the variables themselves are still not at steady-state. Figure 14 illustrates this statement by showing the profiles from Figure 12 generated with $N_x = 3601$, $N_y = 1201$ and $\eta_1 = 0.8$ at different times within this statistically stationary region in Figure 13 (right). Density is still varying in time within this period, something on the order of $O(3 \times 10^{-2} \text{ kg/m}^3)$, which is at least three times larger than the maximum spatial discretization error. This variation between $t = 0.085$ and 0.09 s, however, is $O(3 \times 10^{-3} \text{ kg/m}^3)$, i.e. one order of magnitude smaller and smaller than the maximum spatial discretization error. Probing the temporal behavior of the streamwise velocity at different spatial locations within the compression ramp reveals a more complex scenario, as shown in Figure 15. Although once again it is clear that this velocity component is not yet at steady-state at the corner and $y/L = 0.02$, there is also a high frequency oscillation with a period of approximately 3.3×10^{-4} s. This oscillation is present at all other points probed near the recirculation bubble region, but with different amplitudes. This behavior is still more complex near the shock boundary-layer interaction region (Point 3), where this high frequency oscillation appears to be modulated by a signal with a period that is approximately 6 times larger. Due to the small time step employed, something on the order of $O(3 \times 10^3)$ points per (high frequency) period are used to capture these oscillations. Hence, an appropriate temporal resolution is likely achieved. Even though these results seem to indicate the presence of linear instabilities within the shock and recirculation bubble regions, these oscillations have an amplitude of $O(1 \text{ m/s})$ whereas the spatial discretization error at this same location ($x/L, y/L = (1, 0.02)$) is on the order of $O(40 \text{ m/s})$, which means conclusive statements cannot be provided until additional grid convergence studies are performed. Similar results are observed for test cases CR2, CR3 and CR4, as illustrated in Figures 16 to 18. Hence, no further discussions are provided for these cases. Additional grid refinement studies, required before definitive statements can be made, are currently underway.

IV. Two-dimensional global mode analysis

Despite the obvious questions posed by the temporal content still present in the two-dimensional base flows computed by either of the open source or the in-house codes, it is interesting and instructive to inquire the shape of the global mode that is being damped before a steady state is reached. Motivation for such an analysis is twofold: on the one hand, it is expected to shed light on the origin of the oscillations observed in the steady states computed; on the other hand, it may also contribute to the discussion on the role played by steady laminar separation bubbles as oscillators or amplifiers [25, 26]. Figure 19 presents the amplitude functions of the two velocity components, the density and temperature perturbations. Results are shown in the vicinity of the compression corner since, significantly, it was found that the leading edge region, including the leading edge shock, is steady and does not contribute to the amplitude functions of the global mode. In contrast, what is clearly visible in the results presented, is the intimate connection of the recompression shock and the laminar separation bubble: *the peaks of the amplitude function of the global mode are to be found at these locations*. In other words, instability in the laminar separation will affect shock motion and vice-versa. This result is in line with the findings of the celebrated work of Crouch *et al.* [27] on the origins of buffeting in turbulent transonic flow on two-dimensional wings, where shock oscillations has been associated with linear amplification of a global mode

having its peak at precisely the shock and (mean) separation location. The same result regarding the inter-dependence of shock motion and global instability in a laminar separation bubble has also been documented in the analysis of $Ma = 16$ hypersonic flow in the double-cone junction by Tumuklu *et al.* [28, 29]. The present results indicate that instability analysis of supersonic flow in the compression corner need to consider the recompression shock as an integral part of the analysis.

V. Conclusions

Explicit Euler time marching and second-order spatially accurate OpenFOAM and in-house codes were employed for simulations of the compression ramp problem under laminar conditions previously thought to be stable to two-dimensional absolute/global linear instabilities. Preliminary grid resolution studies appear to indicate that the spatial and temporal grids employed lead to solutions with an accurate enough unsteady behavior. This behavior suggests the presence of linear disturbances between the shock boundary-layer interaction region and the recirculation bubble. Further grid convergence studies are necessary before any conclusive statements about these disturbances can be provided. Two-dimensional global instability analyses, currently underway, are expected to further elucidate this phenomenon. Preliminary two-dimensional global instability analysis has shown that the amplitude functions of the leading damped global modes of compression corner flow peak at the shock and laminar separation region, which implies that the shock should be included in any type of linear stability analysis of the flow at hand, and further underlines the need for accurate numerics in order for reliable predictions to be made.

Acknowledgments

NC and VT gratefully acknowledge support of their work by AFOSR Grant FA9550-17-1-0115 with Dr. Ivett Leyva as Program Officer. Access to the Copper Cray XE6m supercomputer was provided by project AFVAW10102F62 with Dr. Nicholas Bisek as Principal Investigator and is gratefully acknowledged. RS and LA would like to thank the support received from AFOSR (SOARD) Grant FA9550-13-1-0178 with Dr. Ivett Leyva as Program Officer. Any opinions, findings, and conclusions or recommendations expressed in this material are those of the authors and do not necessarily reflect the views of the United States Air Force Office of Scientific Research or the United States Government.

References

- [1] Chapman, D. R., Kuehn, D. M., and Larson, H. K., “Investigation of separated flows in supersonic and subsonic streams with emphasis on the effect of transition,” *NACA Techn. Note 3869*, 1957.
- [2] Chapman, D. R., Kuehn, D. M., and Larson, H. K., “Investigation of separated flows in supersonic and subsonic streams with emphasis on the effect of transition,” *NACA Rep. 1356*, 1958.
- [3] Edney, B., “Anomalous heat transfer and pressure distributions in blunt bodies at hypersonic speeds in the presence of an impinging shock,” *FFA Techn. Rep. 115*, 1968.
- [4] Babinsky, H., and Harvey, J. K., *Shock Wave / Boundary-Layer Interactions*, Cambridge University Press, 2011.
- [5] Gaitonde, D. V., “Progress in shock wave/boundary layer interactions,” *Prog. Aerosp. Sci.*, Vol. 72, 2015, pp. 80–99.
- [6] Collis, S. S., Joslin, R. D., Seifert, A., and Theofilis, V., “Issues in active flow control: theory, control, simulation and experiment,” *Prog. Aero. Sciences*, Vol. 40, No. 4, 2004, pp. 237–289.
- [7] Joslin, R. D., and Miller, D. N., *Fundamentals and Applications of Modern Flow Control*, AIAA Progress in Aeronautics and Astronautics, 521pp., 2009.
- [8] Carter, J. E., “Numerical solutions of the Navier-Stokes equations for the supersonic laminar flow over a two-dimensional compression corner,” Tech. Rep. 385, NASA, 1972.
- [9] Hung, C., and MacCormack, R., “Numerical solutions of supersonic and hypersonic laminar compression corner flows,” *AIAA Journal*, Vol. 14, No. 4, 1976, pp. 475–481.
- [10] Kutler, P., and Vijaya Shankar, V., “Diffraction of a shock wave by a compression corner: I. regular reflection,” *AIAA Journal*, Vol. 15, No. 2, 1977, pp. 197–203.

- [11] Shankar, V., Kutler, P., and Anderson, D., “Diffraction of a Shock Wave by a Compression Corner: Part II-Single Mach Reflection,” *AIAA Journal*, Vol. 16, No. 1, 1978, pp. 4–5.
- [12] Rudy, D. H., Thomas, J. L., Kumar, A., Gnoffo, P. A., and Chakravarthy, S. R., “Computation of laminar hypersonic compression-corner flows,” *AIAA journal*, Vol. 29, No. 7, 1991, pp. 1108–1113.
- [13] Zapryagaev, V., Kavun, I., and Lipatov, I., “High-pressure layer generation in a compression corner at a supersonic flow velocity,” *Fluid Dynamics*, Vol. 49, No. 6, 2014, pp. 819–826.
- [14] Chuvakov, P., Borovoy, V. Y., Egorov, I., Radchenko, V., Olivier, H., and Roghelia, A., “Effect of Small Bluntness on Formation of Görtler Vortices in a Supersonic Compression Corner Flow,” *Journal of Applied Mechanics and Technical Physics*, Vol. 58, No. 6, 2017, pp. 975–989.
- [15] Anderson, J. D., *Hypersonic and high-temperature gas dynamics*, McGraw-Hill, 1989.
- [16] Brooks, G. P., and Powers, J. M., “Standardized pseudospectral formulation of the inviscid supersonic blunt body problem,” *J. Comp. Phys.*, Vol. 197, No. 1, 2004, pp. 58–85.
- [17] Marcantonio, L. F. G., Tamagnoa, J. P., and Elaskara, S. A., “High speed flow simulation using OpenFOAM,” *Mecánica Computacional*, Vol. 31, edited by A. Cardona, P. H. Kohan, R. D. Quinteros, and M. A. Storti, Asociación Argentina de Mecánica Computacional, 2012, pp. 2939–2959.
- [18] Geuzaine, C., and Remacle, J.-F., “Gmsh: a three-dimensional finite element mesh generator with built-in pre- and post-processing facilities,” *Int. J. Numer. Meth. Eng.*, Vol. 79, No. 11, 2009, pp. 1309–1331.
- [19] Balay, S., Abhyankar, S., Adams, M. F., Brown, J., Brune, P., Buschelman, K., Dalcin, L., Eijkhout, V., Gropp, W. D., Kaushik, D., Knepley, M. G., May, D. A., McInnes, L. C., Mills, R. T., Munson, T., Rupp, K., Sanan, P., Smith, B. F., Zampini, S., Zhang, H., and Zhang, H., “PETSc Web page,” <http://www.mcs.anl.gov/petsc>, 2018. URL <http://www.mcs.anl.gov/petsc>.
- [20] Greene, P. T., Eldredge, J. D., Zhong, X., and Kim, J., “A high-order multi-zone cut-stencil method for numerical simulations of high-speed flows over complex geometries,” *Journal of Computational Physics*, Vol. 316, 2016, pp. 652–681.
- [21] Roe, P., “Approximate Riemann solvers, parameter vectors, and difference schemes,” *Journal of Computational Physics*, Vol. 43, No. 2, 1981, pp. 357 – 372.
- [22] Harten, A., “High Resolution Schemes for Hyperbolic Conservation Laws,” *Journal of Computation Physics*, Vol. 47, 1983, pp. 357–393.
- [23] Jiang, G. S., and Shu, C. W., “Efficient Implementation of Weighted ENO Schemes,” *Journal of Computational Physics*, Vol. 126, 1996, pp. 202–228.
- [24] Martin, M. P., Xu, S., and Wu, S. M., “Preliminary Work on DNS and LES of STBLI,” *AIAA*, 2003, pp. 2939–2959.
- [25] Theofilis, V., Hein, S., and Dallmann, U. C., “On the origins of three-dimensionality and unsteadiness in the laminar separation,” *Phil. Trans. Roy. Soc. London A*, Vol. 358, 2000, pp. 3229–3246.
- [26] Theofilis, V., “Global linear instability,” *Annu. Rev. Fluid Mech.*, Vol. 43, 2011, pp. 319–352.
- [27] Crouch, J. D., Garbaruk, A., and Magidov, D., “Origin of transonic buffet on aerofoils,” *J. Fluid Mech.*, Vol. 628, 2009, pp. 357–369.
- [28] Tumuklu, O., Levin, D., and Theofilis, V., “Investigation of unsteady, hypersonic, laminar separated flows over a double cone geometry using a kinetic approach (Editor’s Choice),” *Phys. Fluids*, Vol. 30, 2018, p. 046103.
- [29] Tumuklu, O., Theofilis, V., and Levin, D., “On the unsteadiness of shock–laminar boundary layer interactions of hypersonic flows over a double cone (Featured Article),” *Phys. Fluids*, Vol. 30, 2018, p. 106111.

Appendix

OpenFOAM solvers used

Tables

Elements	p_{\max}/p_{∞}	u_p (m/s)	p_p (Pa)	ρ_p (kg/m^3)	T_p (K)
13061	15.965	117.565	1652969	5.61110	1026.08
53121	16.096	110.735	1658497	5.63049	1025.97
92501	16.220	110.241	1661359	5.63695	1026.56
294241	16.243	110.092	1661655	5.64067	1026.06

Table 1 Convergence history of the inviscid flow over the parabolic cylinder body at $Ma = 3.5$. Results obtained using the midpoint integration rule and a full TVD scheme (Gamma = 1) are shown at $t = 0.1s$ and a probe location ($x_p = -01$, $y_p = 0.1$)

Elements	P_1	P_2	P_3
756834	579.93003	-36.791174	846.937145
3074270	528.98182	-39.992594	848.179798
6949543	523.92066	-40.230205	848.400341

Table 2 Convergence history of the compression ramp flow at $Ma = 3.0$. Steady results for the streamwise component of the base flow velocity, \bar{u} , presented at three probe locations inside the boundary layer, $P_1(x_1 = 5 \times 10^{-5}, y_1 = 10^{-5})$ prior to the laminar separation bubble, $P_2(x_2 = 10^{-3}, y_2 = 10^{-5})$ inside the laminar separation zone at the ramp junction, and $P_3(x_3 = 1.2 \times 10^{-3}, y_3 = 10^{-4})$ on the downstream ramp wall

Total elements	Separation location ($x_{\text{plate}}/L, y/L$)	Reattachment location ($x_{\text{ramp}}/L, y/L$)	$(c_f)_{\min} \times 10^4$
2,282,160	(-0.1752, 0)	(0.2357, 0.2179)	-9.51
5,872,868	(-0.1761, 0)	(0.2375, 0.2182)	-9.56
9,191,310	(-0.1759, 0)	(0.2370, 0.2181)	-9.55

Table 3 Separation location, reattachment location and minimum skin friction coefficient of three different meshes; lengths have been scaled with the flat plate length, $L = 0.06mm$, with the corner being the origin.

Points	p_{\max}/p_{∞}	u_p (m/s)	p_p (Pa)	ρ_p (kg/m^3)	T_p (K)
77361	16.019	93.092	1692577.7	5.7196639	1030.8879
173641	16.2929	94.1229	1690802.0	5.7158835	1030.4876
236181	16.2535	90.6003	1692000.4	5.7165246	1031.1023
481401	16.2428	91.1905	1692732.7	5.7197263	1030.9711

Table 4 Same as Table 1, but for a circular cylinder using the in-house code with generalized coordinates.

Case	Ma	Re	θ (Degree)	p_∞ (Pa)	u_∞ (m/s)	T_∞ (K)	ρ_∞ (kg/m ³)	μ_0 (kg/(m s))
CR1	3.0	1.68x10 ⁴	10	101325	1041.66	300.0	1.17661	0.678101
CR2	3.0	1.3x10 ⁴	20	101325	1041.66	300.0	1.17661	0.876315
CR3	3.0	2.7x10 ⁴	20	101325	1041.66	300.0	1.17661	0.421929
CR4	3.0	4.0x10 ⁴	20	101325	1041.66	300.0	1.17661	0.284802

Table 5 Free stream parameters from compression ramp simulations using in-house code.

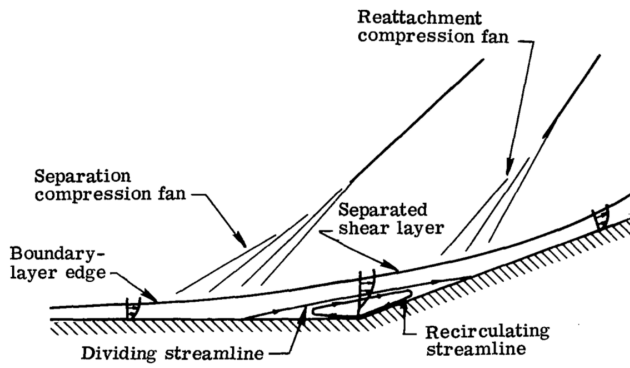


Fig. 1 Schematic representation of the compression corner [8]

Figures

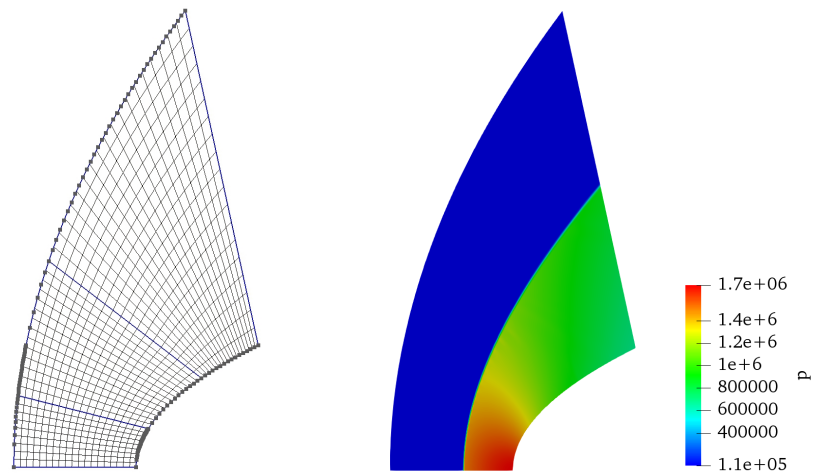


Fig. 2 Structured grid used for the solution of the parabolic cylinder problem (left) and pressure distribution at steady state (right)

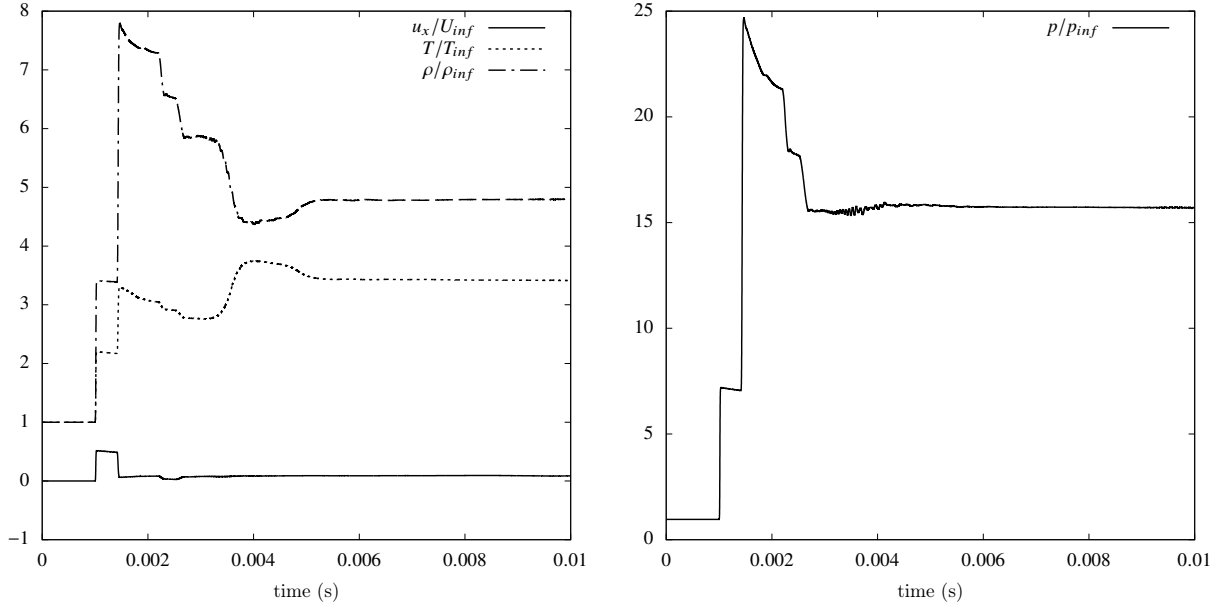


Fig. 3 Development in time of scaled streamwise velocity, temperature and density (left) and pressure (right) at field point $(x_0, y_0) = (-0.1, 0.1)$ in the inviscid flow over the parabolic cylinder body at $Ma = 3.5$, using the inflow values $U_{infty} = 1215.16 \text{ m/s}$, $T_{infty} = 300 \text{ K}$, $\rho_{infty} = 1.1764 \text{ kg/m}^3$ and $p_{infty} = 105660 \text{ Pa}$ to scale the respective quantities

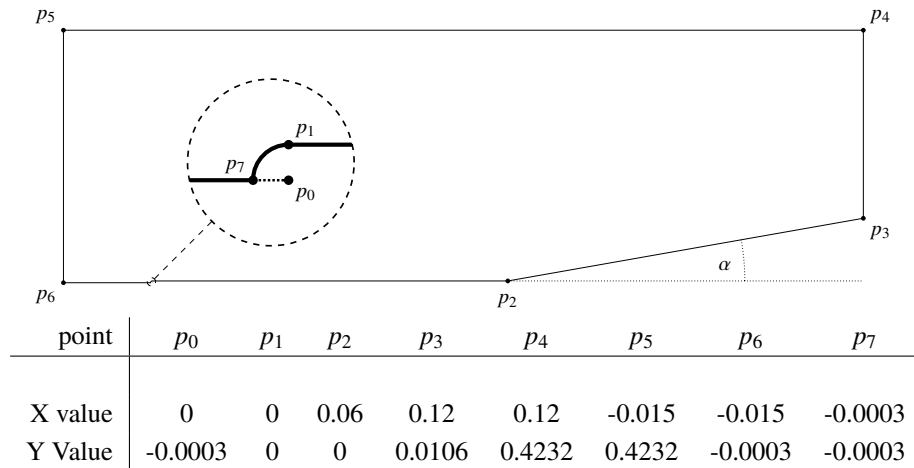


Fig. 4 Schematic of the compression corner geometry used with a ramp angle $\alpha = 10 \text{ deg}$, highlighting the leading edge region. The table defines the coordinates (in m) of the points indicated in the graph.

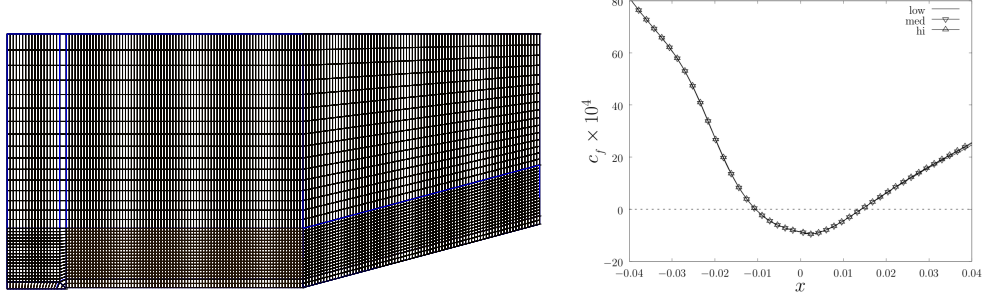


Fig. 5 *Left:* Structured grid used for the solution of flow over a compression ramp. For clarity, a coarse resolution is shown. *Right:* Skin friction distribution in the vicinity of the compression corner.

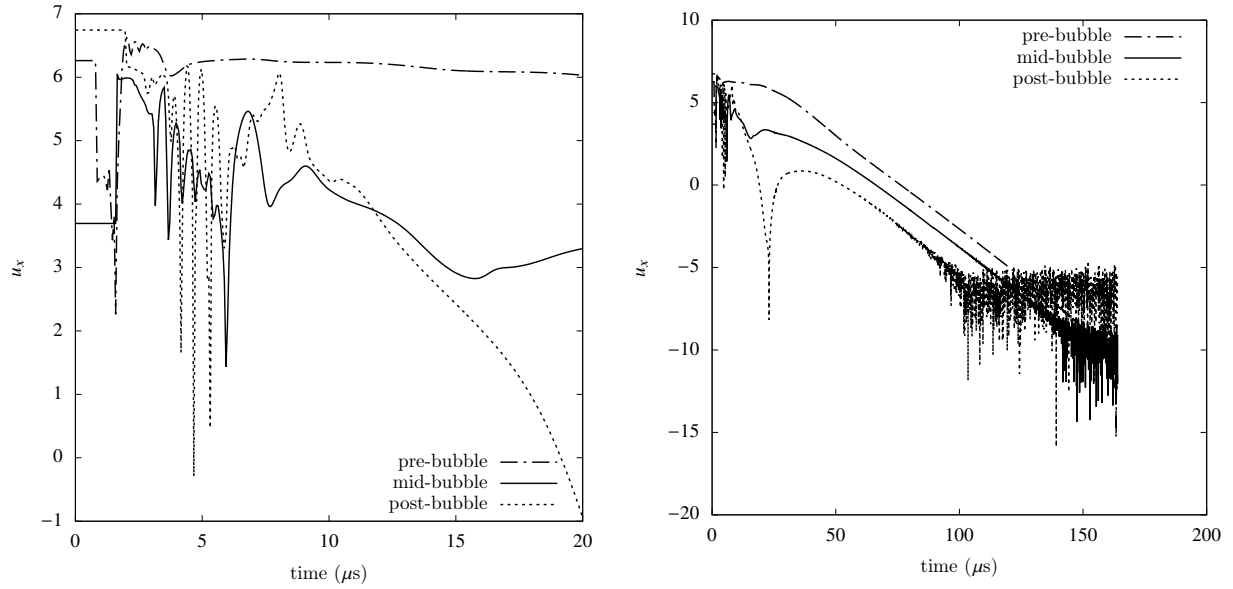


Fig. 6 Short- and long-time development of the streamwise velocity component at three probe locations, prior to the bubble $(x_0, y_0) = (-0.1, 0.1)$, at the ramp junction $(x_0, y_0) = (-0.1, 0.1)$ and at a location after the bubble, $(x_0, y_0) = (-0.1, 0.1)$

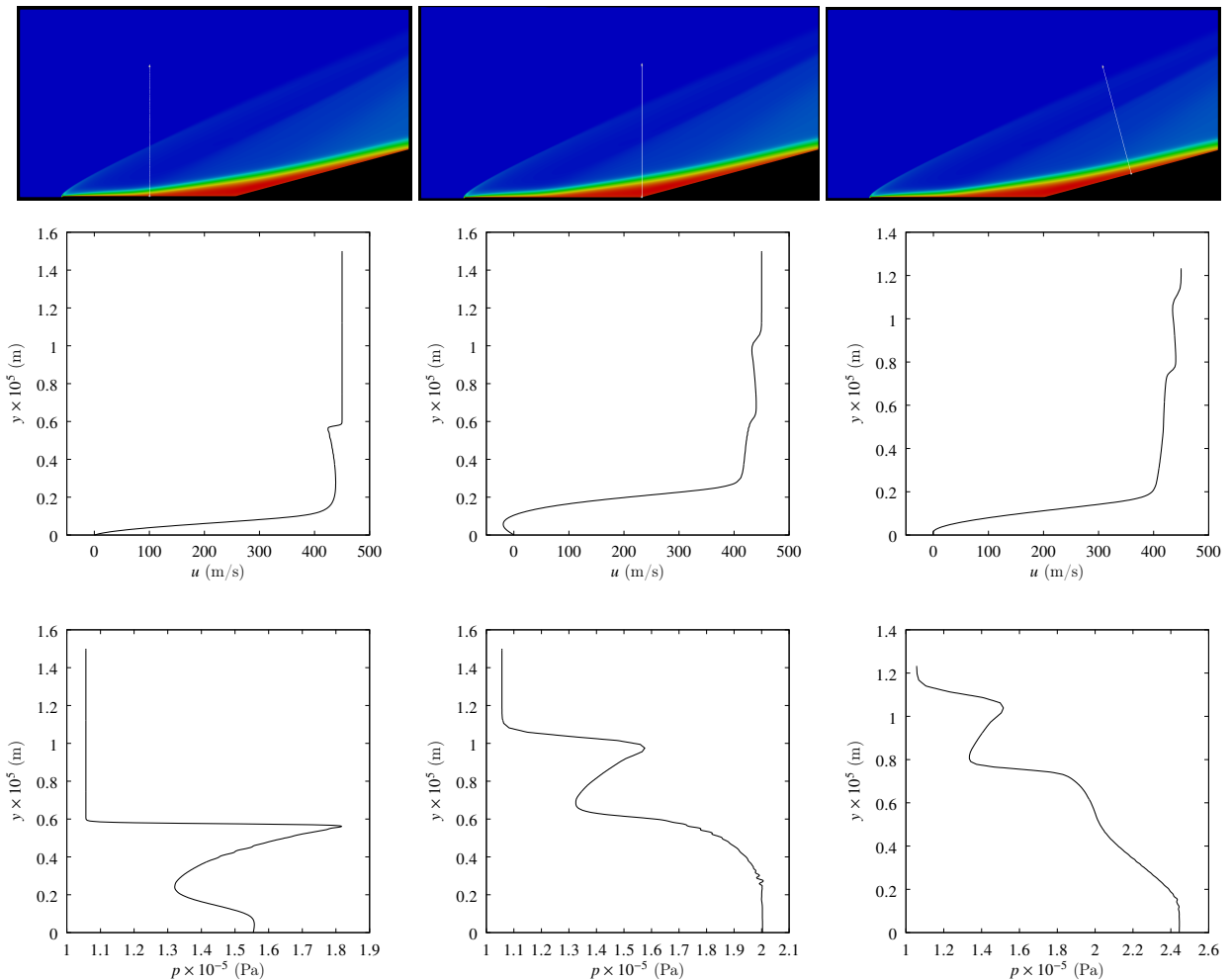


Fig. 7 *Upper row:* Locations on the ramp where profiles were extracted. *Middle row:* Streamwise velocity component profiles. *Lower row:* Pressure profiles.

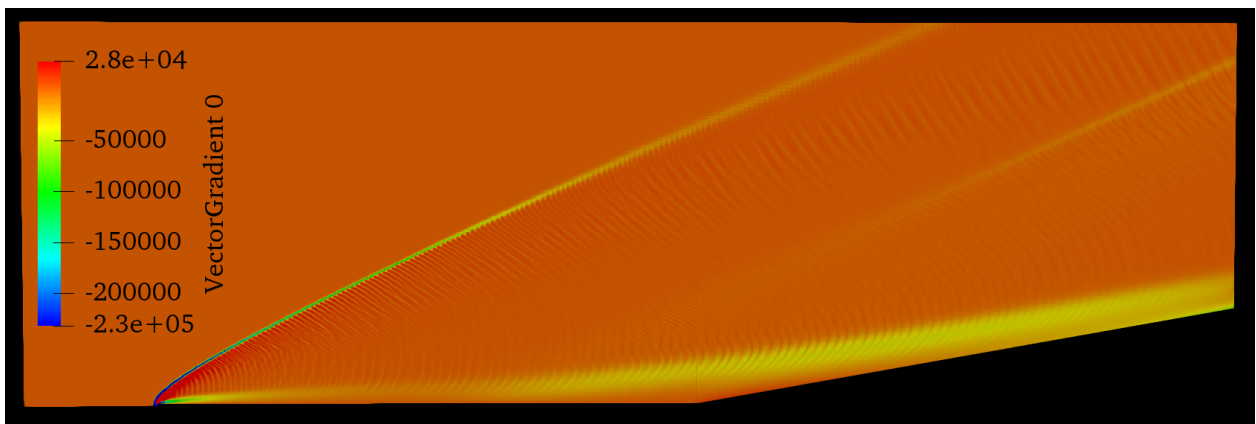


Fig. 8 Gradient of the velocity magnitude of the steady state solution obtained by OpenFOAM in Fig. 7, indicating traces of (well-resolved) small-amplitude perturbations in the entire simulation domain.

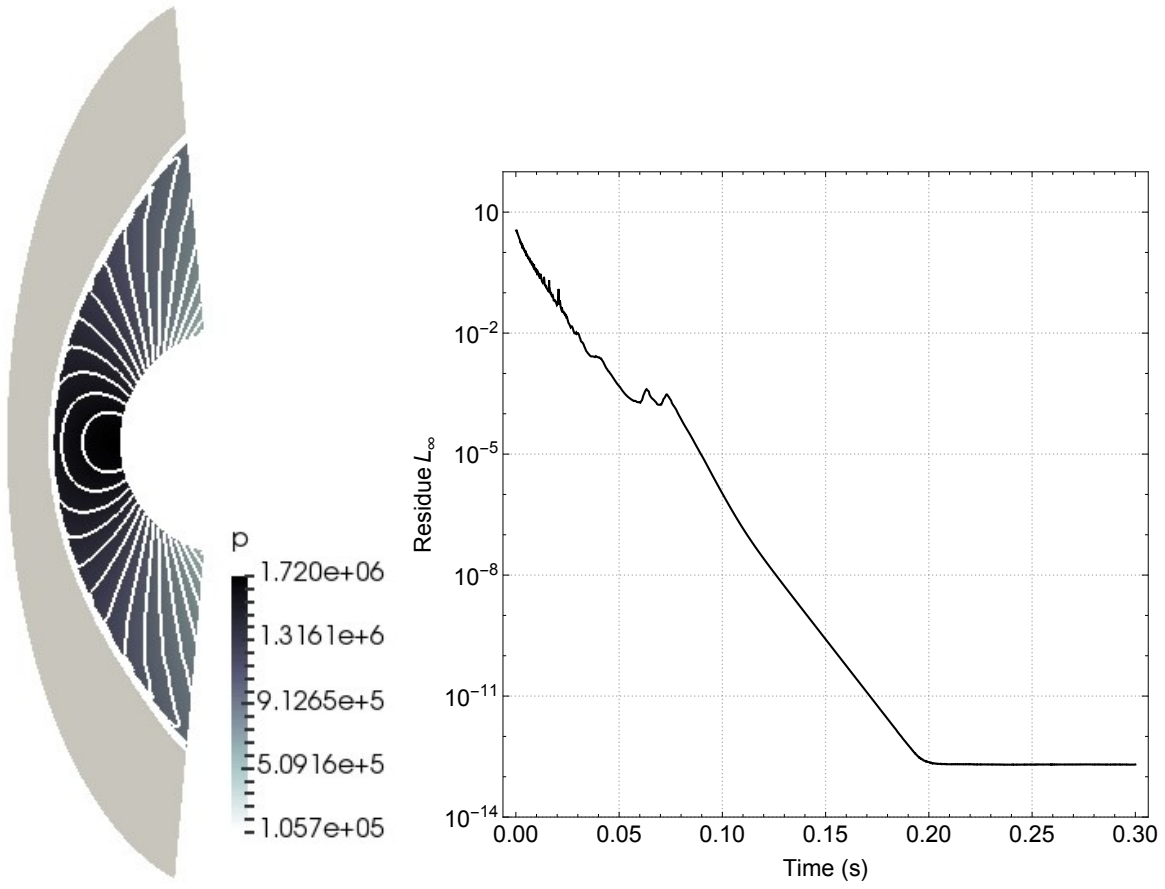


Fig. 9 Pressure distribution with 20 contours and and convergence of the residue under L_∞ norm.

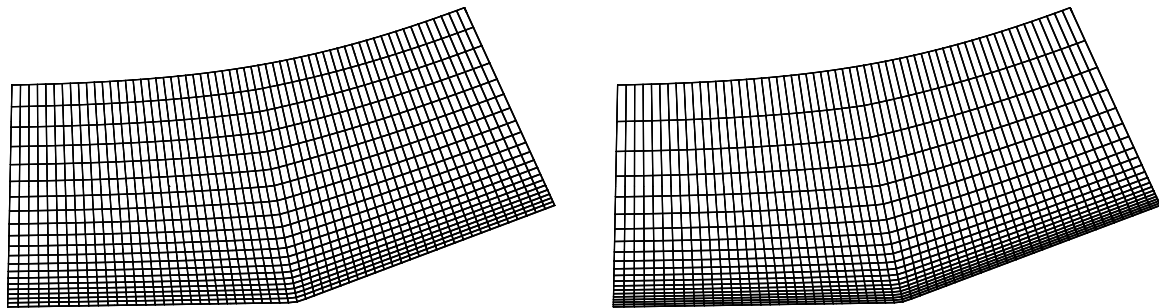


Fig. 10 Structured grid used for the compression ramp simulation in the in-house code, for clarity the number of points are $N_x = 61$ and $N_y = 21$, **Left:** $\eta_1 = 0.7$ and **Right:** $\eta_1 = 0.8$.

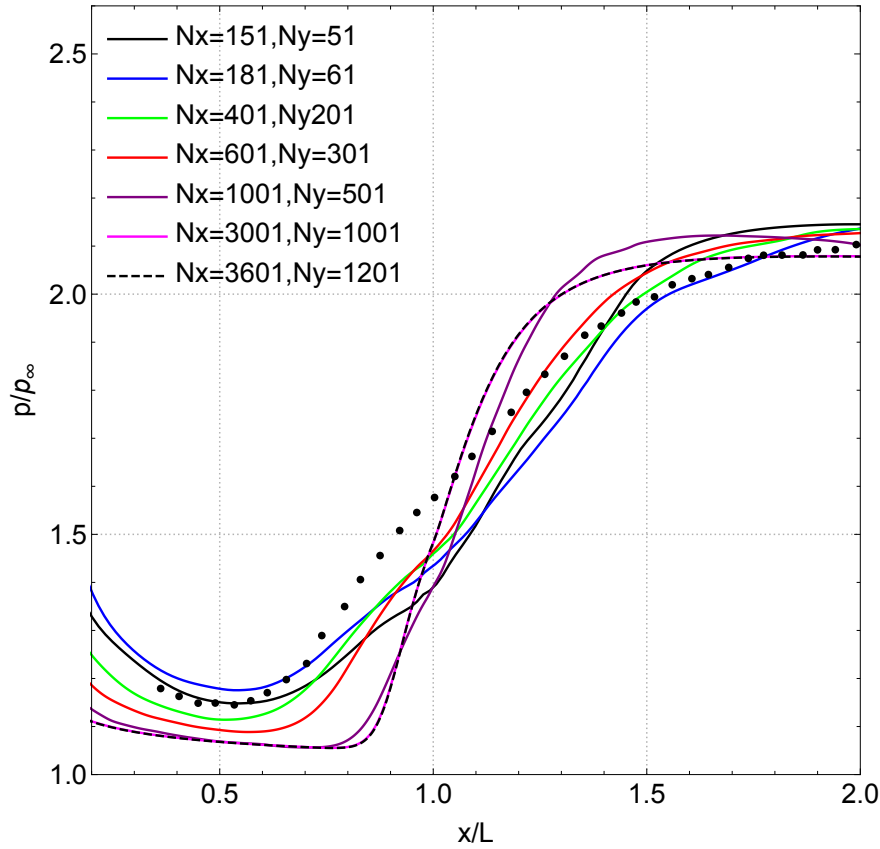


Fig. 11 Wall-pressure distribution for the CR1 test case with $\eta_1 = 0.7$ extracted at $t = 0.05$ s. Points from [8].

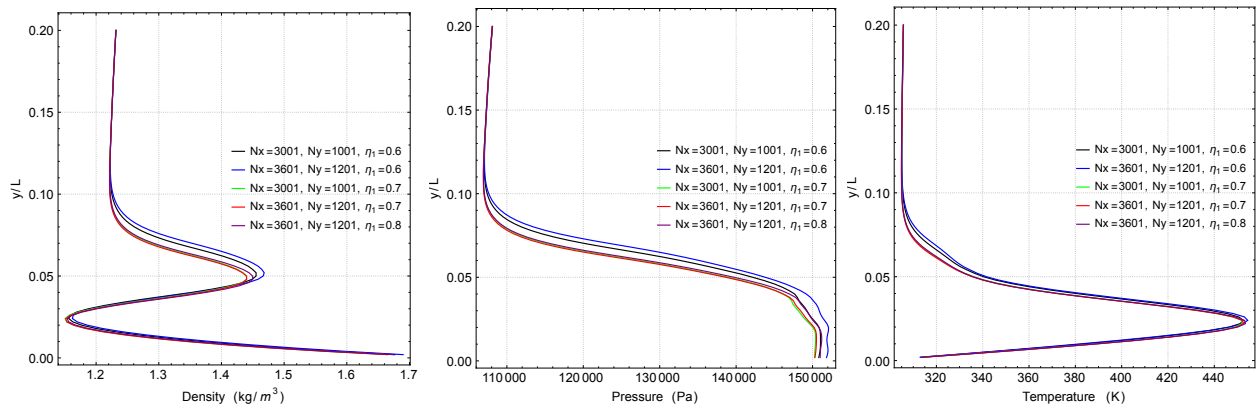


Fig. 12 Density (left), pressure (center) and temperature (right) at the corner ($x/L = 1$) for the CR1 test case extracted at $t = 0.05$ s for different number of grid points and of grid refinement levels.

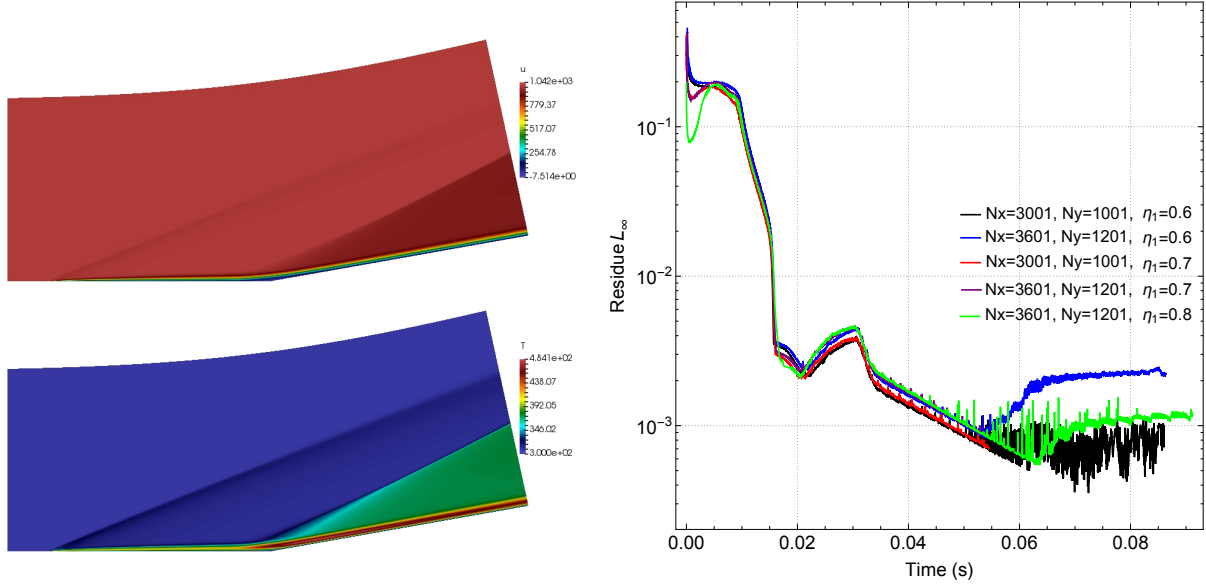


Fig. 13 Case CR1. *Left:* Streamwise velocity (top) and temperature (bottom) with $N_x = 3601$, $N_y = 1201$ and $\eta_1 = 0.8$ extracted at $t = 0.09123$ s, *Right:* Density increment (mass conservation residue multiplied by Δt) maximum norm versus time simulation for different number of grid points and grid refinement levels.

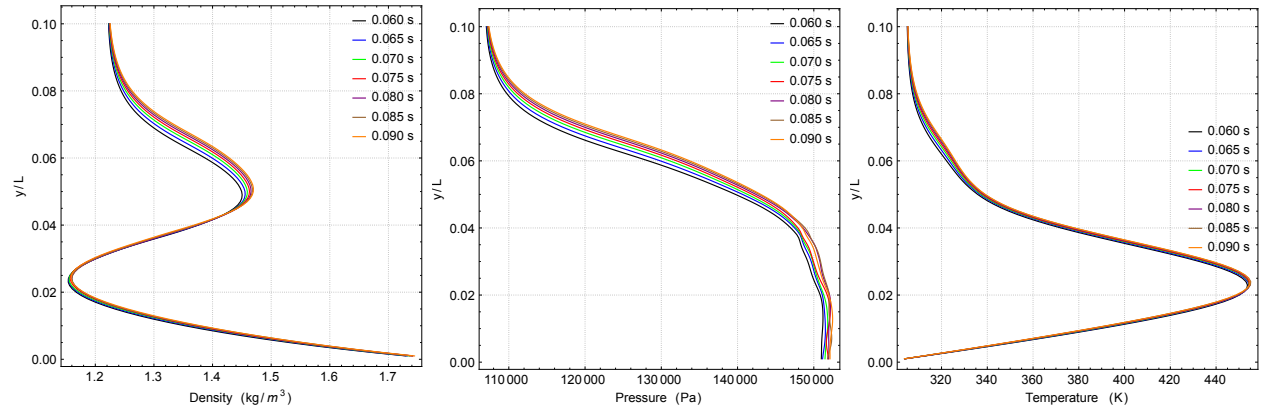


Fig. 14 Density (left), pressure (middle) and temperature (right) versus wall normal direction in CR1 test case for $0.06 \text{ s} \leq t \leq 0.09 \text{ s}$ with $N_x = 3601$, $N_y = 1201$ and $\eta_1 = 0.8$ measured at $x/L = 1$.

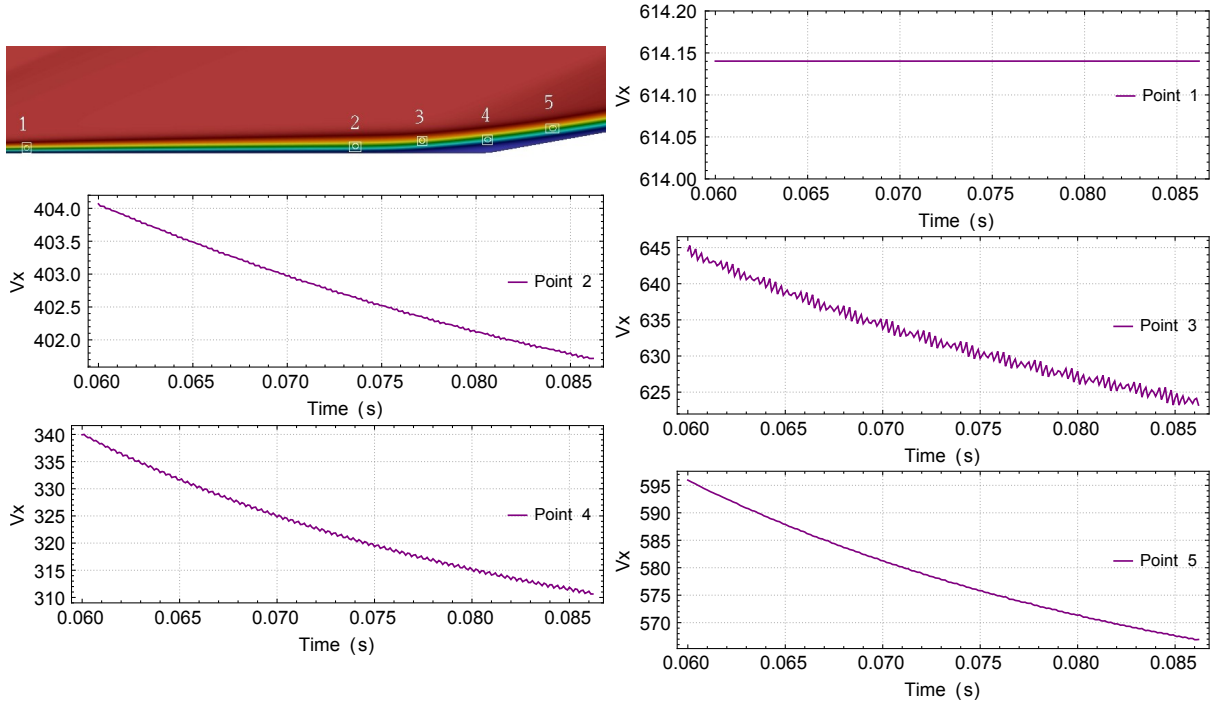


Fig. 15 Streamwise velocity versus time at (x,y) in meters: Point 1 (3.0,0.1), Point 2 (8.0,0.1), Point 3 (9.0,0.2) Point 4 (10.0,0.2) and Point 5 (11.0,0.4) for the CR1 test case with $N_x = 3601$, $N_y = 1201$ and $\eta_1 = 0.6$.

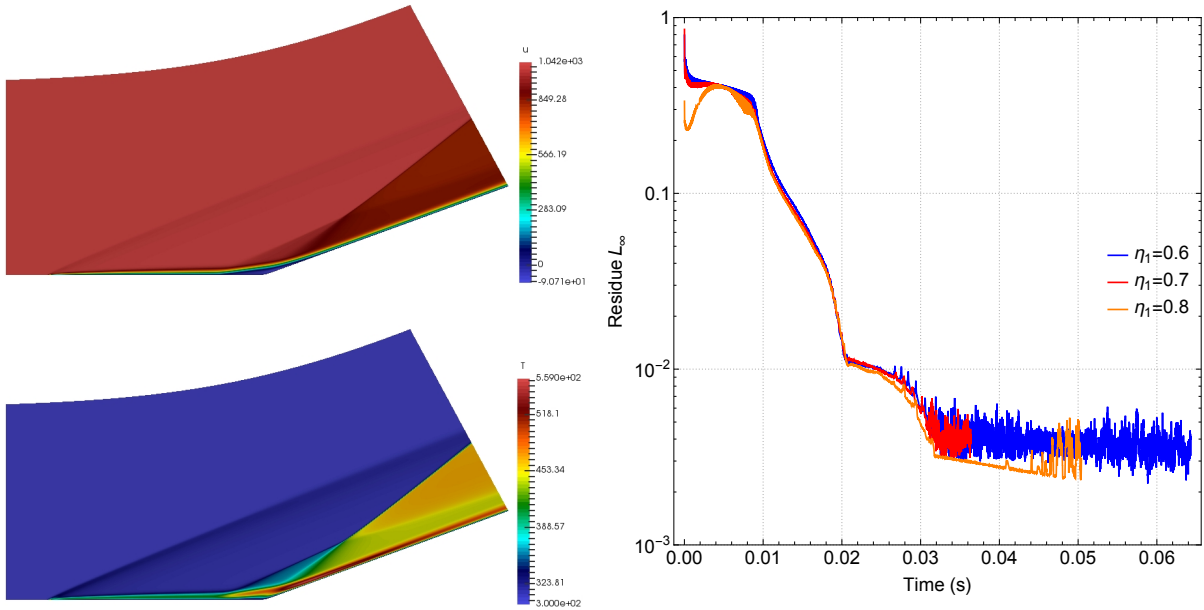


Fig. 16 Case CR2. *Left:* Streamwise velocity (top) and temperature (bottom) with $N_x = 3001$, $N_y = 1001$ and $\eta_1 = 0.8$ extracted at $t = 0.05$ s, *Right:* Density increment (mass conservation residue multiplied by Δt) maximum norm versus time simulation for different grid refinement levels.

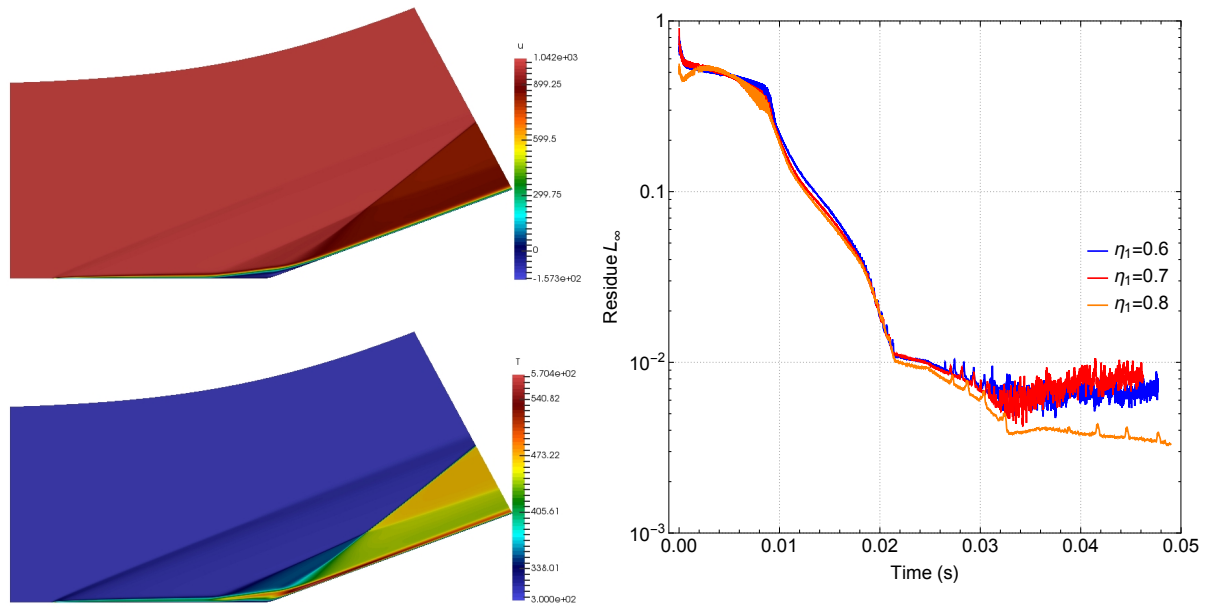


Fig. 17 Same as Figure 16 but for test case CR3.

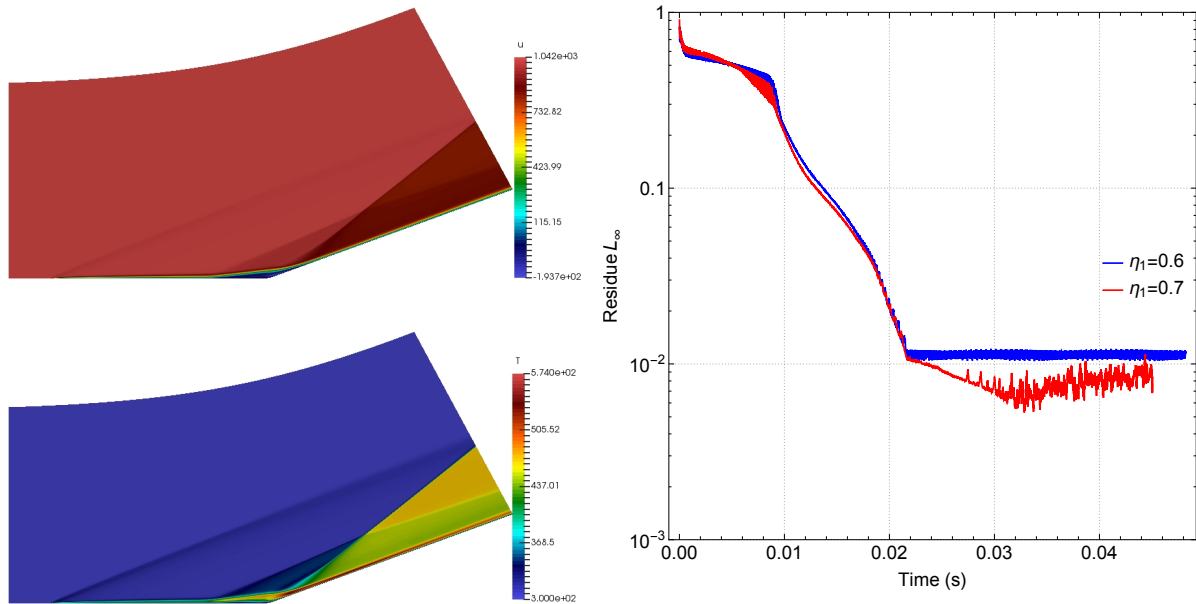


Fig. 18 Same as Figure 16 but for test case CR4 with $\eta_1 = 0.7$ at $t = 0.045$ s.

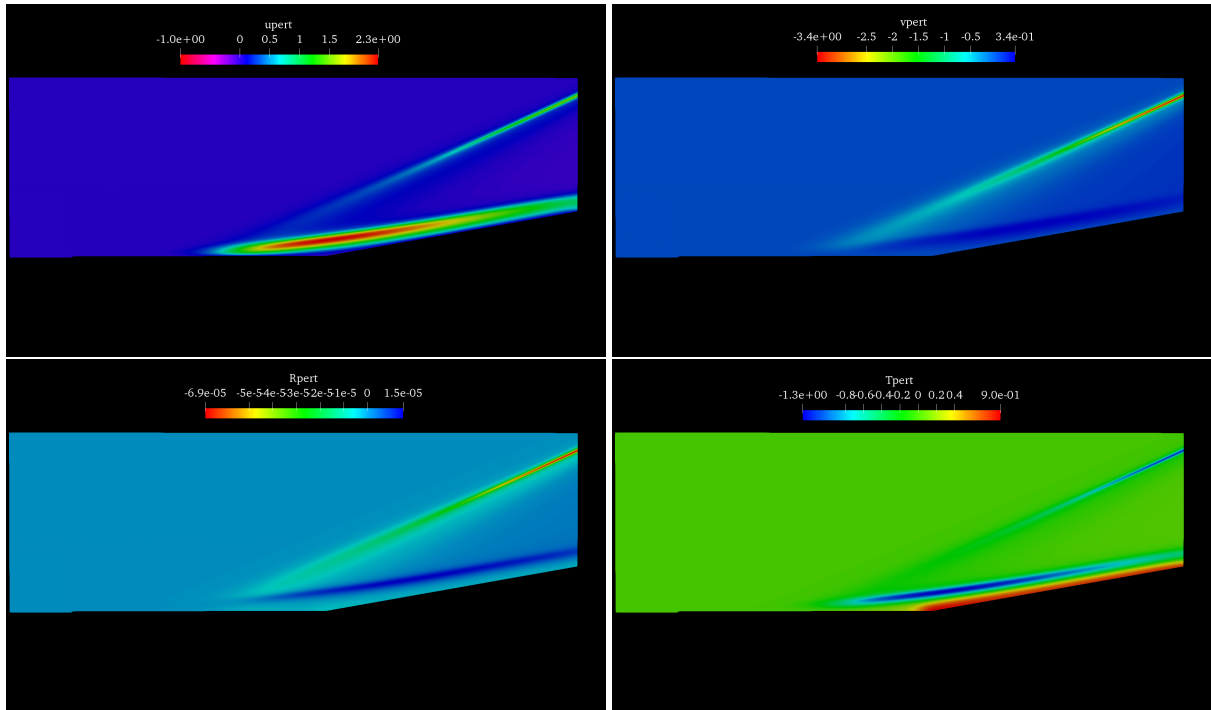


Fig. 19 Amplitude functions of the least-damped global mode at the conditions examined by Carter[8]. *Upper left:* streamwise velocity component, $\hat{u}(x, y)$; *Upper right:* transverse velocity component, $\hat{v}(x, y)$; *Lower left:* perturbation density $\hat{\rho}(x, y)$; *Lower right:* perturbation temperature $\hat{T}(x, y)$;